Geophysical Journal (1989) **98**, 429–446

Seismic representation theorem coupling: synthetic SH mode sum seismograms for non-homogeneous paths

J. Regan
Geological Survey of Canada, 1 Observatory Crescent, Ottawa, Ontario, Canada K1A 0Y3

D. G. Harkrider
Seismological Laboratory 252-21, California Institute of Technology, Pasadena, CA 91125, USA

Accepted 1989 February 7. Received 1989 February 7; in original form 1988 October 3

SUMMARY

In this paper the methods for representation theorem coupling of finite-element or finite difference calculations and propagator matrix method calculations (Harkrider) are developed. The validity and accuracy of the resulting hybrid method are demonstrated. The resulting hybrid technique can be used to study the propagation of any phase that can be represented in terms of an SH mode sum seismogram, across regional transition zones or other heterogeneities. These heterogeneities may exist in regions which form subsegments of a longer, mostly plane-layered, path. Examples of structures of interest through which such waves can be propagated using these techniques include, regions of crustal thickening or thinning such as continent–ocean transitions or basins, anomalous bodies of any shape located in the path, and sudden transitions from one layered structure to another. Examples of the types of phases that may be propagated through these structures include Love waves, L_g, S_n, and S_a.

Key words: coupling, non-homogeneous paths, representation theorem, seismograms

1 INTRODUCTION

The hybrid method is simple in concept. The propagation path is divided into plane-layered segments, and non-plane-layered segments. The non-plane-layered segments may contain arbitrary structures. The propagator matrix (PM) technique is used to propagate the disturbance through the plane-layered segments and the finite element (FE) or finite difference (FD) method is used to propagate it through the non-plane-layered segments. The source is assumed to lie within a plane-layered region. Since neither coupling technique (PM to FE or FE to PM) provides a complete solution if it is applied at the physical boundary between plane-layered and non-plane-layered regions, the FE or FD grid must contain not only the complex region but also segments of each of the plane-layered structures which adjoin the ends of the complex region. Reflections from the complex structure within the grid must be carefully considered when designing the grid (Regan 1987) to ensure that their effects are included in the final solution. The wavefield is propagated from the source to the boundary of the FE or FD grid containing the first complex region using the PM method. The method used to transmit the wavefield across the boundary into the FD or FE grid containing the non-plane-layered region is straightforward (Regan & Harkrider 1989; Regan 1987). The wavefield is then propagated through the non-plane-layered region using the FE or FD method. Next, the wavefield can be transmitted across the boundary between the FD or FE grid containing the non-plane-layered region and the remainder of the second plane-layered region using the representation theorem (RT) integration coupling method developed in this paper. This sequence of procedures can be repeated any number of times so that any number of non-plane-layered regions can be included in the source to receiver path. The RT integration coupling method uses a 2-D Cartesian finite element formulation. Analogous methods for the 3-D case follow directly.

Many methods have been used to model the propagation of seismic disturbances across regions of varying structure such as transition zones. The types of models that have been used to approximate transition regions can be separated into several types which are illustrated in Fig. 1.

The simplest type of model (Fig. 1a) consists of two homogeneous layered regions, 1 1′, and 3 3′ separated by a vertical boundary or a region 2 2′ in which elastic properties vary smoothly. Sato (1961a) derives analytical expressions for the transmitted and reflected waves, the phase and group velocities, and evaluates the approximate reflection and transmission coefficients (R and T) in each case. More recently, Kennett (1973) has developed a numerical technique for solving the problem of seismic waves

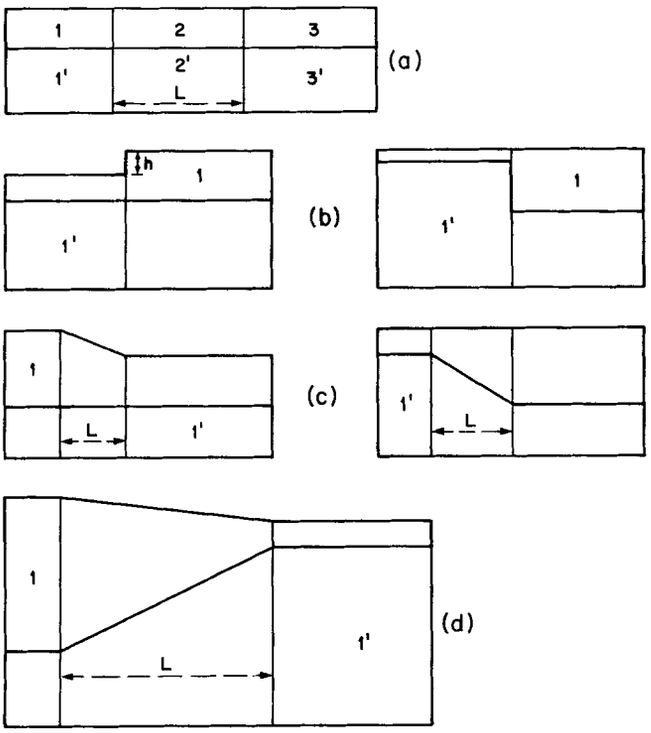

Figure 1. Types of models used in studies of propagation of Love waves across continent–ocean boundaries, in order of increasing complexity; (a) shows two homogeneous layered regions, 1 and 3, separated by an intermediate region, 2, in which elastic properties vary smoothly between their values in regions 1 and 2; (b) shows a layer over a half-space with a step change in the thickness of the layer; (c) shows a model with a smooth change in thickness, either at the surface or the Moho; (d) shows a model with a smooth change in thickness both at the surface and the Moho. The variations in (a), (c), and (d) occur in a transition region of length *L*.

interacting with a layer or layers in which properties change across a surface perpendicular to or at a specified angle from the layering.

The next level of model complexity is the inclusion of a change in the thickness of the surface layer at the discontinuity between the two structures (Fig. 1b). Sato (1961b) obtained analytical solutions and thus approximate expressions for R and T for the special case of a surface step with height h much less than the wavelength of the incident wavefield. Hudson & Knopoff (1964) obtained expressions for more general surface step models. Alsop (1966) developed an approximate method for determining R and T which assumes that all energy remains in Love waves. Gregersen & Alsop (1974, 1976) used an extended form of the method of Alsop (1966, 1968) to show that normal incidence is a good approximation for oblique incidence at angles of incidence of less than 40°. Bose (1975) used an integral equation formulation to yield asymptotic solutions at large distances from the step consistent with results derived for the step models by Regan & Harkrider (1989) using the PM to FE coupling technique that forms part of the overall hybrid technique. Kazi (1978a, b) uses a variational method to show that T increases after the cut-off frequency when the conversion of Love waves to body waves at the surface step is considered. Earlier studies by Alsop (1966) and Knopoff & Hudson (1964) showed that T decreased when the body waves were neglected. Martel (1980) used a FE technique to evaluate propagation of Love waves across a Moho step. Spatial filtering of the transmitted and reflected modes to determine transmission and reflection coefficients allowed the isolation of the diffracted body wave component. The modal filtering technique discussed in this paper would provide a simple way to do such decompositions on FE or FD results determined for any complex structures. Also these structures would not need to be near the end of the propagation path as is the case with a pure FE or FD type calculation.

Studies using the surface step model and the Moho step model have been generalized in several ways. We will discuss only one, replacing the step by a transition region (Fig. 1c). Knopoff & Mal (1967), and Knopoff *et al.* (1970) explained an analytical solution for models of type (1c) when the slope of the surface (or Moho) in the transition region is small. Pec (1967) calculated the dispersion of Love waves propagating in a wedge-shaped layer. Boore (1970) used FD to study the propagation of a simple low frequency Love wave across a transition region (Fig. 1c). He noted that in the region of the transition mode conversions and conversion to other types of waves were important. Lysmer & Drake (1971, 1972) and Drake (1972), use a FE method based on Zienkiewicz & Cheung (1967) which includes a rigid grid bottom and thus allows no energy to escape the grid. The formulation also requires that the incident modal energy is exactly equal to the sum of the reflected and transmitted modal energy. Conversion to body waves is seen as a distortion of the modal eigenfunctions. Lysmer & Drake (1971) use this method to study the effect of a transition of type 1c, or 1d, on the incident fundamental mode Love wave energy. They attribute the differences between their results and those of Boore (1970) to body wave interference in Boore's results. However, conversion to body waves and escape of those body waves from the system defined by the finite element grid play an important role in understanding the propagation of waves across regional variations in structure (Regan & Harkrider 1989). So, in fact, the method of Lysmer & Drake (1972) with its distorted eigenfunctions might be interpreted to be the method containing body wave interference. Thus, the approach used by Boore (1970) and the approach used in the present study will provide more physical insight into the processes of attenuation along complex paths. The method of Lysmer & Drake (1971) also includes a method for calculating 'mode participation factors'. These measure the ratio of the energy of a single mode seismogram incident on the complex region and the resulting energy of each single mode exiting the complex region. Similar ratios can be determined using the Green's function filtering technique presented in the present study. Both methods are based on the Love wave orthogonality relations. Drake & Bolt (1980) used the method of Lysmer & Drake (1972) to study fundamental mode Love waves normally incident on the California continental margin. They conclude that the ocean continent boundary strongly increases the attenuation of fundamental mode Love waves, as Regan & Harkrider (1989) suggest.

All the studies discussed in the previous paragraph used

periods much longer than those that will be considered in the following discussions. Most previous studies considered transition regions with lengths comparable the wavelength of the incident energy. The shorter periods used in this study allow the examination of the effects of transition regions with lengths many times the wavelength of the incident energy. Of all previous studies mentioned above only Kennett & Mykkeltveit (1984) and Bouchon (1981, 1982) have generated realistic seismograms, the latter at regional distances only. Instead, most studies concentrated on measuring phase velocities and transmission and reflection coefficients for individual modes. In this study the input energy is in the form of seismograms containing a sum over a range of modes for fundamental and overtone Love waves. This approach produces a realistic output seismogram which can be filtered and decomposed to yield the transmission and reflection coefficients if they are needed. In light of these facts it is clear that the results derived using the method developed in the present paper can provide a significant improvement in the understanding of the propagation of L_g waves and other phases that can be expressed in terms of mode sum seismograms.

2 THE RT INTEGRATION METHOD FOR FE TO PM COUPLING

To clearly explain the method used to couple finite element and propagator matrix methods, it is useful to first discuss some of the foundations on which each method is based, and to explain the basic concepts inherent in the use of the representation theorem. In Section 2.1 the representation theorem will be discussed, and the assumptions that lead to the form of the representation theorem used in this study will be presented. The theory used to derive the version of the PM technique used in the present study is explained in detail by Harkrider (1964). The notation and the basic concepts of the PM technique needed to explain the representation theorem integration coupling technique developed in the present paper are summarized in Section 2.2. The FE method used in this study is an extensively modified version of the stress waves in solids code (Frazier, Alexander & Petersen 1973). The result is an explicit time domain FE method using a rectangular grid, and the hourglass correction terms which the rectangular grid necessitates (Kosloff & Frazier 1978; Regan 1987). The FE method can be driven by a source distant from the finite element grid, as outlined by Regan & Harkrider (1989). Displacement or stress time histories can be recorded at any node or element centre in the grid. Given these time histories further details of the particular implementation of the FE method are not important to the understanding of the coupling technique. The implementation of the RT coupling technique will be discussed in Section 2.3. A method for determining the accuracy of the RT coupling results will be presented in Section 2.4. A method for modal Green's function filtering of finite element or hybrid results is developed in Section 2.4. Finally, in Section 3, all aspects of the method are tested using a simple model which enables the calculation of PM synthetics for direct comparison to the hybrid results.

2.1 The representation theorem and Green's functions

The basis of the method used to couple the results of a finite element calculation into the PM calculation is the application of the representation theorem on the boundary between the regions in which each method is used. The representation theorem relates the displacement at any point, ζ, in a volume V to the body forces f_i acting within V and to the displacements u_i and the tractions T_i acting on the surface S of V. There are many equivalent ways of expressing the representation theorem, for example (Aki & Richards 1980, eq. 2.41)

$$u_p(\mathbf{x},t) = \int_{-\infty}^{+\infty} d\tau \iiint_V f_i(\zeta,\tau) G_{ip}(\mathbf{x}, t-\tau; \zeta, 0)\, dV(\xi) + \int_{-\infty}^{+\infty} d\tau \int_S \int \Big(G_{ip}(\mathbf{x}, t-\tau; \xi, 0) T_i[\mathbf{u}(\xi,\tau), n_j] - c_{ijkl} \frac{\partial}{\partial x_l} G_{kp}(\mathbf{x}, t-\tau; \xi, 0) u_i(\xi,\tau) n_j \Big)\, dS(\xi) \quad (1)$$

where ξ is the location of a point on S, $\mathbf{x}$ the location of a receiver in V, $u_p(\mathbf{x},t)$ is the p component of the displacement at time t at $\mathbf{x}$, t is the observation time, τ is the source time, n_j is the jth component of the outward unit normal to S, $T_i[u(\xi,\tau), n_j] = \tau_{ij} n_j = (u_{i,j} + u_{j,i}) n_j$ and $u_i(\xi,\tau)$ are the boundary conditions specifying stress and displacement as a function of source time τ for all points ξ on S, and G_{ip} is the Green's function which represents the displacement in the ith direction at $\mathbf{x}$ at time t due to a unit impulse applied in the pth direction at position ξ at time τ.

The general form of the representation theorem given above is not suitable for demonstrating how the coupling of the FE and PM methods is accomplished. To transform it to a more manageable form it is assumed that no body forces are present within volume V, and that the medium is isotropic. Applying both conditions allows the representation theorem to be written as follows.

$$u_p(\mathbf{x},t) = \int_{-\infty}^{+\infty} d\tau \int_S \int \{ G_{pi}\tau_{ij} + \lambda G_{pl,l} u_j + \mu(G_{pi,j} + G_{pj,i}) u_i \} n_j\, dS(\xi) \quad (2)$$

where all derivatives are with respect to ξ.

For the case of SH waves only, eq. (2) can be further simplified to

$$u_2(\mathbf{x},t) = \int_0^{\infty} d\tau \int_S \int \mu(\xi_3) \{ G_{22} u_{2,k} + G_{22,k} u_2 \} n_k\, dS(\xi), \quad (3)$$

For the 2-D SH solutions at $\mathbf{x}$ in V, eq. (3) is integrated from $-\infty$ to ∞ over the variable ξ_2. The representation theorem becomes (de Hoop 1958)

$$u_2(\mathbf{x},t) = \int_0^{\infty} d\tau \oint_C \mu(\xi_3) \{ \Gamma_{22} u_{2,k} + \Gamma_{22,k} u_2 \} n_k\, dC(\xi_1, \xi_3) \quad (4)$$

where C is the curve defined by the intersection of the surface S with the x_1–x_3 plane, $\mu(\xi_3)$ is the rigidity at the depth ξ_3, and the half-space Green's functions Γ_{22} and the forcing functions $u_2(\xi_1, \xi_3, t)$ satisfy the initial conditions

$$u_2 = u_{2,k} = \Gamma_{22} = \Gamma_{22,k} = 0 \qquad t \le \tau \quad (5a)$$

the radiation conditions,

$$u_2 \to 0 \quad u_{2,k} \to 0 \quad \text{as} \quad \xi \to \infty \tag{5b}$$

and the boundary conditions,

$$u_{2,z} = \Gamma_{22,z} = 0 \quad \text{at} \quad z = 0. \tag{5c}$$

Following the notation of de Hoop (1958) the half-space Green's function is

$$\widetilde{\Gamma_{22}}(\mathbf{x}, s; \boldsymbol{\xi}) = \int_{-\infty}^{+\infty} \widetilde{G_{22}}(\mathbf{x}, s; \boldsymbol{\xi})\, d\xi_3 = \frac{1}{2\pi\rho\beta^2}[K_0(sa^-/\beta) + K_0(sa^+/\beta)] \tag{6}$$

where $a^{\pm} = \sqrt{(x_1 - \xi_1)^2 + (z \pm \xi_3)^2}$. To compare this form for the Green's functions with the forms of the displacements used in the rest of this discussion it is first necessary to transform equation (6) from the Laplace transform domain to the Fourier transform domain. Applying the change of variables, $s = i\omega$, and transforming the modified Bessel functions, K_0, into Hankel functions gives

$$\overline{\Gamma_{22}}(\mathbf{x}, \omega; \boldsymbol{\xi}) = \frac{-i}{4\mu}[H_0^{(2)}(k_\beta a^+) + H_0^{(2)}(k_\beta a^-)]. \tag{7}$$

This form is analogous with the displacement solution for the line source in a half-space:

$$\overline{u_y}(\mathbf{x}, \omega) = \overline{u_y}(r, \phi, z) = \frac{i\pi}{2}[H_0^{(2)}(k_\beta a^+) + H_0^{(2)}(k_\beta a^-)]. \tag{8}$$

Thus,

$$\overline{u_y}(r, \phi, z) = -2\pi\mu\overline{\Gamma_{22}}(\mathbf{x}, \boldsymbol{\xi}) \tag{9}$$

and the displacement Green's function can be calculated in a manner similar to the displacement solution. The line source displacements and the line source Green's functions differ only by a multiplicative factor of $-2\pi\mu$.

2.2 The propagator matrix technique

To implement the representation theorem integration coupling algorithm for coupling finite element results into propagator matrix calculations it is first necessary to obtain and evaluate expressions for the displacement and stress seismograms and the stress and displacement Green's functions used in the representation theorem integral (equation 4). Evaluation of displacement and/or stress Green's functions ($\overline{\Gamma_{22}}$, $\overline{\Gamma_{22,1}}$, $\overline{\Gamma_{22,3}}$) is necessary in all applications of the RT integration coupling method regardless of whether the forcing functions are FE results, analytical stress and displacement seismograms evaluated using PM or other techniques, or stresses and displacements from other sources. However, the PM stress seismograms are used in the following discussions only as an example of a well-defined and easily evaluated form of forcing functions. Using a single plane-layered model for all segments of the path and stress and displacement PM seismograms ($\overline{u_2}$, $\mu\overline{u_{2,1}}$, $\mu\overline{u_{2,3}}$) as forcing functions produces RT integration results (hybrid seismograms) which may be directly compared with synthetics generated using only a single PM calculation. Synthetics generated for comparison to hybrid results by using a single PM calculation will be referred to as pure propagator matrix seismograms (PPM).

For the SH problem in Cartesian coordinates the expressions that need to be considered are for $\overline{\Gamma_{22}}$, $\overline{\Gamma_{22,1}}$, $\overline{\Gamma_{22,3}}$, $\overline{u_2}$, $\overline{\sigma_{xy}}$, and $\overline{\sigma_{zy}}$. For the geometry (Fig. 2) used to couple surface waves from a finite element grid into a layered medium, through which the waves will be transmitted by convolution with propagator matrix generated Green's functions only the $\overline{\Gamma_{22}}$, $\overline{\Gamma_{22,1}}$, $\overline{u_2}$, and $\overline{\sigma_{xy}}$ are used. However, $\overline{\Gamma_{22,3}}$ and $\overline{\sigma_{zy}}$ will also be derived for completeness. Should the geometry change so that it would be necessary to integrate over a horizontal surface such as the bottom of the grid then $\overline{\Gamma_{22,3}}$ and $\overline{\sigma_{zy}}$ would also be used.

The stresses $\overline{\Gamma_{22,1}}$, $\overline{\Gamma_{22,3}}$, $\overline{\sigma_{xy}}$, and $\overline{\sigma_{zy}}$ can be expressed in terms of spatial derivatives of displacements. Evaluating the numerical derivative gives a reasonable approximation to the desired stress values. However, a more direct, and more efficient, method for determining the values of the stresses is to evaluate the analytical expression for each stress derived from the corresponding analytical displacement expressions. The displacement and stress expressions for double-couple sources, line sources, and line source Green's functions are

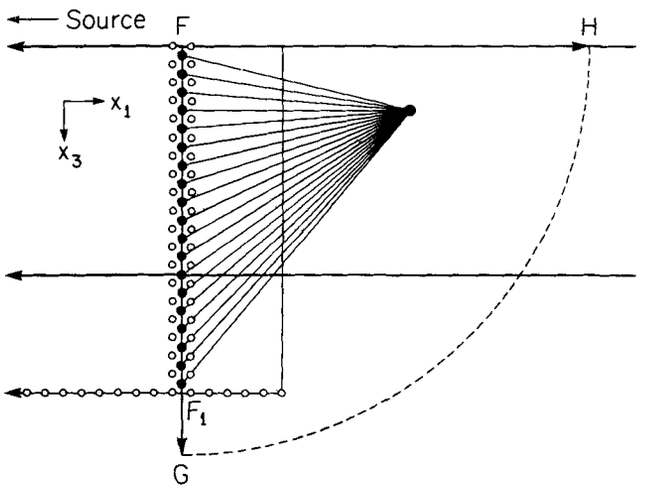

Figure 2. Geometry of FE to PM coupling. The two long horizontal lines show the free surface and the boundary between a layer and a half-space. The short vertical and horizontal lines show the boundaries of the finite element grid. The FE grid continues off the figure to the left. The open circles within the grid and along its bottom boundary represent nodes in the finite element grid. The solid circles represent element centres where the forcing functions $u_2(t)$ and $\sigma_{12}(t)$ are recorded during the FE calculations. The integration path of the representation theorem integral, C, is illustrated as the closed curve FGHF. The arrows at G and H indicate that the $x_1 = x$ coordinate at H and the $x_3 = z$ component at G both tend to infinity. The large dot within contour G denotes a receiver. The lines connecting the element centres (filled dots) and this receiver denote the line source Green's functions which propagate the forcing functions to the receiver. The line FG denotes the boundary between the 'complex' region to its left, and the 'simple' region to its right. The finite element grid extends into the 'simple' region to provide numerical stability.

presented in terms of propagator matrix notation in the Appendix. The evaluation of these expressions is accomplished using a generalized version of Harkrider's (1964) PM codes. The general form of the expressions and the propagator matrix notation used in the remainder of the present paper are summarized below.

The basic idea behind the propagator matrix method as implemented by Harkrider (1964, 1970) is to transmit the disturbance produced by a source within a layered half-space structure through that structure by combining terms that describe the source, the medium response, and the propagation effects. The terms that apply the effects of the propagation path in the z direction are in the form of propagator matrices. For source and receiver both at depth, they are separated into two parts, the propagation in z from the source to the surface, and the propagation in z from the surface to the receiver. An additional propagation term adds the effect of the propagation in the r coordinate. In most cases the general form of a modal displacement at a receiver at depth is

$$v(r, \phi, z) = S\underline{A}_L\left[\frac{v_S(h)}{v_0}\right]_H\left[\frac{v_R(z)}{v_0}\right]_H P \qquad (10)$$

where S is a function of the source strength and geometry, $\underline{A}_L$ represents the medium response for a surface source and a surface receiver, P expresses the propagation effects in direction r,

$$\left[\frac{v_S(h)}{v_0}\right]_H$$

is the term for transmitting the disturbance from the source depth to the surface which because of reciprocity can be expressed as a modal propagator from the surface to the source depth h, and

$$\left[\frac{v_R(z)}{v_0}\right]_H$$

is the propagator from the surface to the receiver depth. The subscript H denotes homogeneous, that is independent of and not containing a source. The terms within the square brackets represent matrix quantities, not simple ratios. If the source is a stress source rather than a displacement source then

$$\left[\frac{v_S(h)}{v_0}\right]_H$$

is replaced by

$$\frac{k_L}{\mu(h)}\left[\frac{\tau^*(h)}{\dot{v}_0/c_L}\right]_H,$$

where $\mu(h)$ is the rigidity at the depth of the source. If stress rather than displacement is to be recorded at the receiver, then

$$\left[\frac{v_R(z)}{v_0}\right]_H$$

is replaced by

$$\frac{k_L}{\mu(z)}\left[\frac{\tau^*(z)}{\dot{v}_0/c_L}\right]_H,$$

where z is the depth of the receiver.

2.3 FE to PM coupling

In the present study, a simple geometry, consisting of the same layer over a half-space for all segments of the path, is used as a test case to illustrate the method and assess its accuracy. The geometry of the simple problem is illustrated in Fig. 2. The coupling of FE seismograms into a layered media through which they are transmitted by the PM technique and the application of the representation theorem is accomplished by direct evaluation of the representation theorem integral as given in equation (4). The evaluation of the representation theorem integral on the contour, FGH (Fig. 2), will be discussed in three parts. First, the quantities used in the evaluation of the representation theorem integral on the subsegment FG of the contour, FGH, will be discussed. Then, the procedure used to estimate the value of this integral along FG will be explained. Finally, it will be shown that the contributions to the representation theorem integral from integration along segments GH and HF of the contour, FGH, are zero.

Before the particulars of the integration procedure can be discussed, each of the quantities in equation (4) must be defined. The integration surface for the segment FG is a line with the x-coordinate held constant, only the terms generated by setting $k = 1$ in equation (4) need to be considered. Thus, the quantities of interest are, μ, u_y, σ_{xy}, Γ_{22}, and $\Gamma_{22,1}$. The displacement and stress seismograms at the element centres, illustrated as dots in Fig. 2, are recorded during the FE calculation. The element centre displacement u_y, and the element centre stress, σ_{xy}, are used as the u_2 and $\mu u_{2,1}$ terms, respectively. Line source Green's functions are calculated for the transmission of a unit line displacement, applied at each of the element centres illustrated as dots in Fig. 2, to the receiver point. These displacement and stress Green's functions, calculated using the PM method, are the Γ_{22}, and $\mu\Gamma_{22,1}$ terms in equation (4).

The representation theorem integral is evaluated using trapezoidal rule numerical integration of equation (4) along segment FG of contour FGH. The displacement and stress seismograms, and the displacement and stress Green's functions are time series. The time spacing between successive points in each time series is the time step duration, Δt, used in the FE calculation. Similarly, the distance between integration points along the integration surface is Δz, the grid spacing within the finite element grid. It should be remembered that the terms $\Gamma_{22}u_{2,k}$ and $\Gamma_{22,k}u_2$, in the representation theorem integral, equation (4), are convolutions. Thus, the products of the Green's functions and FE results, $\bar{\Gamma}_{22}\bar{u}_{2,k}$ and $\bar{\Gamma}_{22,k}\bar{u}_2$, are calculated in the Fourier transform domain, then, inverse Fourier transformed into the time domain and summed. Integration along the segment FG of the contour, FGH, is approximated by numerically integrating along the subsegment FF_1 of the segment FG, and assuming that the

contributions to the integral from the remainder of segment FG are negligible. The assumption that no significant contribution is made by integration along segment F_1G can be justified for the case where F_1 is chosen so that the earliest possible arrival of energy from a source at depth F_1 is later than the last arrival in the seismogram being considered. The uncertainties introduced when this criterion is not satisfied will be assessed in the next section. For the remainder of this discussion we will assume that the depth F_1 illustrated in Fig. 2 satisfies this criterion.

Next, the integration over the remaining two segments of the contour, C, will be shown to give no contribution to the representation theorem integral. The segment of the contour FH, along the free surface will be considered first. The integration surface for the segment FH of the contour, C, is a line with the z-coordinate held constant. Thus, only terms generated by setting $k = 3$ in equation (4) need to be considered. The free surface boundary condition applied on this surface states that at $z = 0$ the stress, $\mu u_{2,3}$, is zero. Since the Green's function, Γ_{22}, used in all the calculations also satisfies the free surface BC, the Green's function stress, $\mu\Gamma_{22,3}$, is also zero at $z = 0$. Therefore, one term in each product in the integrand of equation (4) is zero, causing the value of the integral along this portion of the contour, C, to be zero. Next, the segment GH of the contour, C, will be considered. As $\xi \to \infty$ the displacements u_2 and $u_{2,k}$ must approach zero since the radiation condition is satisfied. Again, one component of each product in the integrand of equation (4) is zero. Clearly, this makes the integrand zero and verifies that the section GH of contour, C, makes no contribution to the representation theorem integral.

Before summarizing the method one further simplification in the evaluation of the representation theorem integral will be presented. The integration of equation (4) along a vertical surface equivalent to contour FG can be expressed as

$$u_2(\mathbf{x}, t) = \int_0^\infty \mu(\xi_3)[\Gamma_{22}(x, z; \xi_1, \xi_3)u_{2,1}(\xi_1, \xi_3) + \Gamma_{22,1}(x, z; \xi_1, \xi_3)u_2(\xi_1, \xi_3)]n_k \, d\xi_3. \quad (11)$$

The forcing functions, $u_2(\xi_1, \xi_3)$ and $\mu(\xi_3)u_{2,1}(\xi_1, \xi_3) = \sigma_{xy}$ can be expressed in terms of the variables used in the PM method. For the line source this is done by substituting expressions from the Appendix, eqs (A10) and (A11b), respectively, for $u_2(\xi_1, \xi_3)$ and σ_{xy}. The line source Green's functions, Γ_{22} and $\mu(\xi_3)\Gamma_{22,1}$ can be expanded in terms of PM variables by substituting equations (A12) and (A13b) for Γ_{22} and $\Gamma_{22,1}$, respectively. Performing these substitutions, and bringing all terms not dependent on ξ_3 out of the integral, yields equation (12a). For a point double-couple source the substitutions for the Green functions are unchanged. For the strike-slip point double-couple source, equations (A4) and (A8b) are substituted for u_2 and σ_{xy} to yield equation (12b). For the dip-slip point double-couple source equations (A5) and (A9b) are substituted for u_2 and σ_{xy} to yield equation (12c).

$$\overline{u_2}(x, z) = \frac{-4\pi i\mu(h)\, e^{-ik_L x}}{k_L}\left[\frac{v_S(h)}{v_0}\right]_H\left[\frac{v_R(z)}{v_0}\right]_H A_L^2 \times \int_0^\infty \mu(\xi_3)\left[\frac{v_R(\xi_3)}{v_0}\right]_H\left[\frac{v_S(\xi_3)}{v_0}\right]_H d\xi_3 \quad (12a)$$

$$\overline{u_2}(x, z) = \frac{2M_0}{\omega}\mathrm{H}_2\left[\frac{v_S(h)}{v_0}\right]_H\left[\frac{v_R(z)}{v_0}\right]_H A_L^2 \times \int_0^\infty \mu(\xi_3)\left[\frac{v_R(\xi_3)}{v_0}\right]_H\left[\frac{v_S(\xi_3)}{v_0}\right]_H d\xi_3 \quad (12b)$$

$$\overline{u_2}(x, z) = \frac{2M_0}{\omega\mu(h)}\mathrm{H}_1\left[\frac{v_S(h)}{v_0}\right]_H\left[\frac{v_R(z)}{v_0}\right]_H A_L^2 \times \int_0^\infty \mu(\xi_3)\left[\frac{v_R(\xi_3)}{v_0}\right]_H\left[\frac{v_S(\xi_3)}{v_0}\right]_H d\xi_3 \quad (12c)$$

where

$$\mathrm{H}_\nu = e^{-ik_L(x-\xi_1)}\left.\frac{\partial H_\nu^{(2)}(k_L r)}{\partial r}\right|_{r=\xi_1} \approx \sqrt{\frac{\xi_1}{r}}\left.\frac{\partial H_\nu^{(2)}(k_L r)}{\partial r}\right|_{r=x}.$$

For all the types of sources discussed in the present paper both convolutions in the integrand of equation (11) produce identical expressions. Thus, it should be possible to accelerate the numerical evaluation of equation (11) by doubling the result of the integration of either convolution. This approach makes it unnecessary to record both displacement and stress seismograms in the FE calculations. Either one of these should be sufficient to calculate a 2-D SH representation theorem integral. This approach also allows the value of the representation theorem integral to be determined using half the number of the Green's functions. The representation theorem integral will be evaluated by doubling the value of the first term in equation (11).

In summary, the procedure used to propagate mode sum seismograms along a path that may include one or more segments of non-plane-layered structure within a longer plane-layered path will be described below, and, for clarity, illustrated in the flow diagram in Fig. 3. The details of the FE to PM coupling technique discussed in this section will be emphasized in this description (see points (2)–(6) below), and its relation to the complete hybrid propagation technique will be demonstrated. The method can be broken down into eight steps.

(1) Choose a source type, a source depth, h, and a horizontal propagation distance, Δ_s, from the source to the finite element grid edge. This distance Δ_s is slightly less than the horizontal distance, Δ_{c_1}, from the source to the edge of the first complex region. Also choose Δz, the vertical spacing between nodes in the finite element grid, and n, the number of nodes in a column in the finite element grid. The quantities n, Δz, and Δ_s, are chosen when designing the finite element grid containing the complex region (Regan & Harkrider 1989, Regan 1987). Use the parameter source type, h, n, Δ_s, and Δz, to generate a vertical section of PM seismograms containing one seismogram at the location of each node in the first column of the finite element grid. This set of seismograms will be called the FE forcing functions.

(2) The FE forcing functions are used as displacement time history constraints on the first column of finite element nodes. This passes the wavefield into the finite element grid providing a complete solution at every node within the finite element grid. A vertical section of displacement seismograms is recorded at a column of finite element centres a horizontal distance, Δ_{FE}, from the beginning of the finite element grid. This set of seismograms will be called the RT forcing functions. $\Delta_s + \Delta_{FE}$ is slightly larger than the

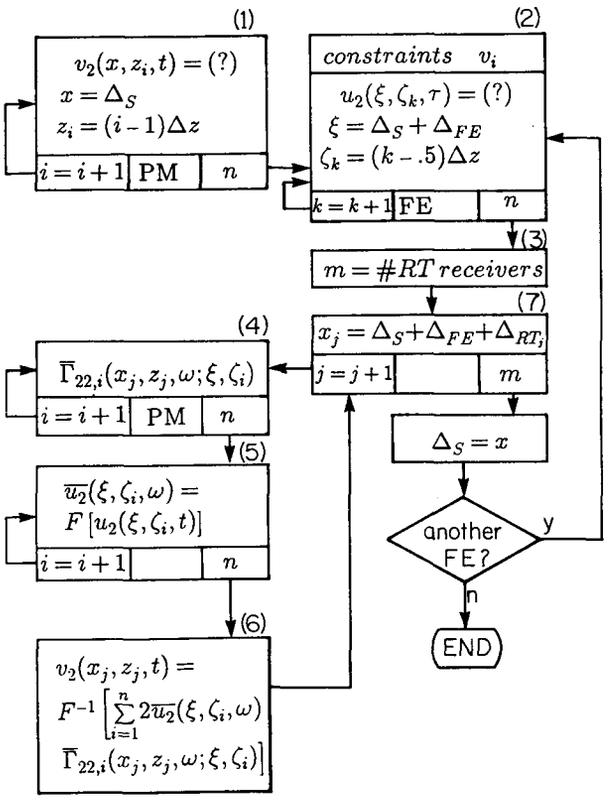

Figure 3. A flow diagram of the generation of a hybrid synthetic mode sum seismogram. The numbers in parentheses above some boxes relate the procedure within that box to a step number in the summary of the method in the text. To avoid double subscripts in the figure $\boldsymbol{\xi} = (\xi, \zeta)$, and $\mathbf{x} = (x, z)$. As in the text, a bar over a quantity indicates the Fourier transform of that quantity. The three small boxes along the bottom of boxes (1), (2), (4), and (5) indicate a loop. The variable in the left-most box indicates the incremented variable in the loop. The centre box is used to indicate the technique used to calculate the quantity. The right-most box shows the largest possible value of the increment variable.

horizontal distance from the source to the end of the region of complex structure and Δ_{FE} is chosen when designing the finite element grid.

(3) Choose the number, j, and locations, (x, z), of desired receivers. The horizontal distance between a receiver and $\Delta_s + \Delta_{FE}$ is Δ_{RT}. If the path from $\Delta_s + \Delta_{FE}$ to the final receiver locations contains another complex region a complete depth section of hybrid seismograms is needed and $j = n$, and $\Delta_{RT} \leq \Delta_{c_n} - (\Delta_s + \Delta_{FE})$. The horizontal distance from the source to the edge of the next finite element grid is Δ_{c_n}.

(4) Calculate line source stress Green's functions. One Green's function is calculated to transmit the disturbance at each element centre to a receiver.

(5) Fourier transform the displacement seismograms in the set of RT forcing functions.

(6) For each element centre, multiply the displacement seismogram from the set of RT forcing functions with the stress Green's function which transmits that displacement seismogram to the receiver. Then, add the resulting product seismograms for all element centres on the depth section and multiply the resulting sum by $2\Delta z$. Inverse Fourier transform the result to give the time domain displacement seismogram at a receiver.

(7) Repeat steps (4)–(6) for each of the j receivers chosen in (3). If another complex region lies in the path from the locations of j to the final receivers this repetition will produce a new set of FE forcing functions. Otherwise the final solution has been reached.

(8) Repeat steps (2)–(7) to propagate across the next complex region.

2.4 Uncertainty estimates and modal filtering for RT coupling

As stated in Section 2.3, the evaluation of the representation theorem along path FG (Fig. 2) is in practice, carried out only along subsegment FF_1. The contributions to the representation theorem integral from integration along subsegment F_1G are assumed to be zero. To insure that the contribution from F_1G is zero, the earliest possible arrival from a source at depth F_1 must be later than the end of the hybrid seismogram being calculated. To rigorously apply this condition, when a seismogram duration of 55 s, a reasonable duration for L_g at $\Delta_s = 1000$ km, is used requires that F_1 lie at a depth in excess of 250 km. FE calculations extending to such depths would be prohibitive. At larger distances the L_g seismogram has even longer durations requiring the integration surface to extend yet deeper. Thus, it is desirable to assess the size of the contributions along subsegment F_1G when the depth of F_1 is considerably smaller than would ideally be the case, and to determine the minimum values of the depth F_1 that will result in acceptable solutions. Fortunately, it is straightforward to derive a simple relation expressing the mode by mode accuracy for a given F_1, and grid spacing (Δz). This relation can be simply and rapidly evaluated before RT integration coupling is attempted. The mode by mode uncertainty estimates can then be used to assess the effect of a particular choice of F_1, Δz, and the time spacing on the accuracy of the hybrid synthetics and to choose optimal values for F_1 and Δz.

To derive the expression for mode by mode integration accuracy we return to the expression of the representation theorem integral along FG in terms of propagator matrix notation (equation 12). Comparing the quantities outside the integral, in each equation in (12), with the expression for displacement due to the corresponding source in a layered medium, equation (A10) to equation (12a), equation (A4) to equation (12b), and equation (A5) to equation (12c), allows equation (12) to be rewritten as

$$u_2(\mathbf{x}, t) = u_2(\mathbf{x}, t) * 2A_L \int_0^\infty \mu(\xi_3)\left[\frac{v_R(\xi_3)}{v_0}\right]_H \left[\frac{v_S(\xi_3)}{v_0}\right]_H d\xi_3. \tag{13}$$

Define I_1 to be the relation

$$I_1 = \int_0^\infty \mu(\xi_3)\left[\frac{v_R(\xi_3)}{v_0}\right]_H \left[\frac{v_S(\xi_3)}{v_0}\right]_H d\xi_3. \tag{14}$$

This immediately leads to the relation

$$2A_L I_1 = 1. \tag{15}$$

Evaluation of this simple equation provides a direct estimate of the accuracy of the integration on a mode by mode basis.

The estimate of the accuracy is obtained by evaluating the I_1 integrand at each integration point used in the RT integration, for each frequency on each branch of the dispersion curve used. For each single frequency mode the quantity on the left hand side of equation (15) is determined at each integration point and summed over the integration surface. If the solution were perfect with no error present, then the sum would be exactly one. In practice the sum departs from one by some amount which gives an estimate of the size of the minimum error that could be expected in that mode in the RT integration results. The estimate is a minimum since it does not account for the phase of the arrivals nor for possible errors in that phase. The evaluation of the error using this relation is much faster than comparing results from multiple applications of RT integration coupling.

An additional result obtained from equation (14) allows a simple method of modal filtering to be defined. It is well known that if i and j represent two different modes for a given period, ($k_i \neq k_j$ for $\omega_i = \omega_j$), then the orthogonality relation for Love waves states that

$$\int_0^\infty \mu(z) v_i(z) v_j(z)\, dz = 0 \qquad i \neq j. \tag{16}$$

Comparing equations (16) and (14), and equating

$$v_i = \left[\frac{v_R(\xi_3)}{v_0}\right]_H,$$

and

$$v_j = \left[\frac{v_S(\xi_3)}{v_0}\right]_H$$

shows that equation (13) is a form of the orthogonality relation. At this point it is useful to notice that the two

$$\left[\frac{v.(\xi_3)}{v_0}\right]_H$$

terms in the equation (13) each have separate origins. One originates with the forcing functions and the other with the Green functions. Thus, any single modes not common to both the

$$\left[\frac{v_R(\xi_3)}{v_0}\right]_H$$

term from the forcing function and the

$$\left[\frac{v_S(\xi_3)}{v_0}\right]_H$$

term from the Green's function will produce zero contribution to the resulting hybrid result. This implies that the only modes present in both the Green's functions and the forcing functions will be present in the RT integration results. Thus, choosing Green's functions with a subset of the modes present in the forcing function will produce a filter that gives RT integration results that contain only that subset of modes.

3 RT COUPLING OF ANALYTIC SEISMOGRAMS AND GREEN'S FUNCTIONS

In this section the validity and accuracy of the numerical implementation of the representation theorem integration coupling technique will be discussed in detail. In the following discussions a seismogram resulting from a RT integration will be referred to as a hybrid seismogram. However, since the representation theorem integral can be evaluated regardless of the method used to generate the forcing functions, easily generated PM forcing functions are used in most tests of the accuracy of the coupling technique, rather than more computationally intensive FE forcing functions. A single test using FE forcing functions is presented for completeness. All the numerical experiments discussed below use the same layer over a half-space model for all portions of the path allowing hybrid results to be directly compared with PPM results. In all cases the layer has a thickness of 32 km, an SH wave velocity 3.5 km s^{-1}, and a density 2.7 g cm^{-3}. The half-space has SH wave velocity 4.5 km s^{-1} and density 3.4 g cm^{-3}.

In the following sections the results of tests of several aspects of the representation theorem integration coupling technique and Green's function filtering will be presented. First, the estimation of uncertainties is discussed, and the values of Δz, Δt and F_1 are chosen. Then, results of the RT integration for the fundamental mode and for each of the first five overtones are presented to illustrate where the discrepancies between the RT results and the analytical results originate. Mode sum results for a line source and for a point source are then presented. Modal filtering of FE or hybrid results is then discussed, and examples of its efficiency are presented. Before these results can be discussed the sets of forcing functions and Green's functions used in the tests need to be explained.

The forcing functions used are the displacement and stress seismograms for a source depth of 8 km. They are evaluated at positions corresponding to the element centres of the right-most column of elements in a FE grid with horizontal and vertical spacing of 0.5 km, whose right-hand edge lies $\Delta_s = 1500.25$ km from the source. Thus, the seismograms are evaluated at points along a vertical surface 1500 km from the source, at depth intervals of 0.5 km, beginning at a depth of 0.25 km below the surface. Separate sets of forcing functions were generated for the fundamental mode and for each of the first five higher modes. Also, an additional set of forcing functions was calculated by summing over the fundamental and the first five higher modes. Single mode and mode sum forcing functions were determined for both a line source and a strike-slip point source. Similarly mode sum and single mode Green's functions were evaluated for a line source at each of the locations where displacement and stress forcing functions were evaluated for a line source at each of the locations where displacement and stress forcing functions were determined and a receiver at the surface. Single mode and mode sum Green functions for a propagation distance of $\Delta_{RT} = 100$, and mode sum Green functions for propagation distances of $\Delta_{RT} = 50$, 100, 150, 250, 500, and 1000 km are used. The representation theorem integration surface for all RT integration examples extended to a depth of 50 km.

3.1 Analysis of uncertainties

Before representation theorem integration calculations are performed it is useful to consider the choices of Δt, the time step in the displacement and stress seismograms, Δ_z, the spacing between integration points, and F_1, the vertical

extent of the integration surface. Once a desired level of accuracy has been defined and the highest frequency to be modelled has been chosen a reasonable set of values for these parameters can be determined. The values of Δz and F_1 are selected using the mode by mode estimator of accuracy discussed in Section 2.4. The tolerated level of uncertainty, $U = 1 - 2A_L I_1$, in the representation theorem integrations described in the present paper is 2 per cent. The translation of this tolerance level to values of Δz and F_1 is discussed below. The integral I_1, equation (14), used to estimate the accuracy of the representation theorem integration is independent of Δt. The value of Δt is chosen so that $1/2\Delta t$ exceeds the highest frequency used in the time series. In practice it is inadvisable to use a value of Δt which is larger than half the minimum travel time for travelling the distance Δz, since this may cause increased errors at the shortest periods.

The effects of varying Δz were studied. Estimations of accuracy were determined for several values of F_1 and Δz. The resulting values of U were examined to determine the effect of changing Δz on the value of U. The results of this examination indicate that $U \approx U_0 \Delta z$, where U_0 is the uncertainty using $\Delta z = 1$ km. The choice of an acceptable value of Δz requires examination of the actual values of U. Table 1 shows the values of U for a small selection of periods on each branch of the dispersion curve. The uncertainty estimation which produced Table 1 used $\Delta z = 0.5$ km, and $F_1 = 50$ km, the values used in the RT integration tests below. These values of Δz and F_1 produce errors below $U = 0.02$ for most modes. The pattern of the variation of U with period seen in this table is typical of all the sample combinations of Δz and F_1 examined. The mode by mode values of U for each separate overtone, and for the fundamental show that U is small and approximately constant until the value of F_1 is reduced to a value comparable to λ, the wavelength for the mode being considered. Further reduction of F_1 causes rapid increases in the value of U.

The effects of varying F_1 were also investigated. The values of U for several values of F_1 at each value of Δz were reexamined to determine the effect of changing the value of F_1 on the value of U. The period below which no uncertainty estimates exceeded 2 per cent was determined for each F_1. The resulting minimum values of T for each F_1, and for $U_0 = 0.4$, and $\Delta z = 0.5$, are plotted in Fig. 4. The curves in Fig. 4 are model-dependent and must be determined for each model used. All values of F_1 below the fundamental

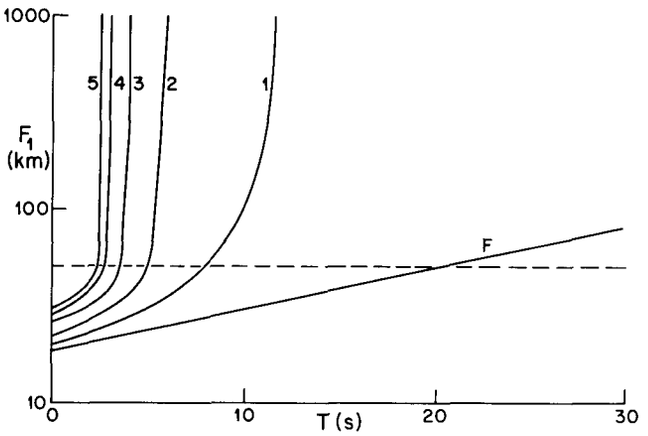

Figure 4. RT integration uncertainty estimates for $\Delta z = 0.5$ km. F_1 is the depth of the deepest integration point on the RT integration surface in kilometres. T is the period of the mode. Each curve is labelled to indicate which overtone it refers to. F refers to the fundamental mode, 1 to the first overtone, etc. Each curve is the locus of points (T, F_1), where T is the maximum period for which a mode can be accurately reconstructed ($U \leq 0.02$) using RT integration to a depth F_1. The horizontal dotted line indicates the 50 km value of F_1 used in the tests of the RT integration technique.

Table 1. RT integration uncertainty estimates

Period	$U = 1 - 2A_L I_1$					
(s)	Fund.	1st	2nd	3rd	4th	5th
500.0000	0.9948					
90.0000	0.8456					
60.0000	0.6726					
30.0000	0.1732					
20.0000	0.0234					
14.0000	0.0069					
11.4000		0.4701				
10.0000	0.0124	0.3129				
8.0000	0.0135	0.0212				
6.0000	0.0142	0.0098				
5.7000			0.3940			
4.0000	0.0148	0.0135	0.0091			
3.8000			0.0102	0.3003		
2.8000				0.0093	0.0526	
2.5000		0.0147	0.0136	0.0112	0.0046	
2.2000				0.0125	0.0091	0.0047
2.0000	0.0152	0.0149	0.0143	0.0132	0.0109	0.0056
1.6000	0.0154	0.0151	0.0148	0.0142	0.0131	0.0112
1.2001	0.0154	0.0153	0.0151	0.0148	0.0143	0.0136
0.8001	0.0154	0.0154	0.0154	0.0152	0.0151	0.0148
0.4000	0.0158	0.0155	0.0155	0.0158	0.0155	0.0154
0.2000	0.0190	0.0159	0.0161	0.0147	0.0156	0.0161
0.1000	0.0130	1.7330	0.0096	0.0085	0.0080	0.0078

mode curve produce uncertainty estimates in excess of $U = 0.02$, the specified cut-off level. The values of F_1 which fall below the part of a given overtone curve that is not near vertical produce uncertainty estimates in excess of $U = 0.02$ for that overtone. The almost vertical portions of the overtone curves, which have periods near the cut-off frequency of the overtone, indicate the values of F_1 that produce acceptable values of U for all periods. Fig. 4 provides a good way to estimate the minimum acceptable value of F_1. Examining Fig. 4 for a given choice of F_1 on a overtone by overtone basis helps to predict and explain the causes of the inaccuracies noted below in the actual RT integration results. The value of F_1 chosen for use in the tests of the RT integration is 50 km, and is indicated by a dotted line in Fig. 4. This value is the minimum value of F_1 that produces acceptable values of U for the longer period modes on the overtone curves. The intersections of the $F_1 = 50$ km line and the curve for each mode indicates the expected uncertainties. The second through fifth overtones should be accurately represented at all periods. The first overtone will introduce somewhat higher uncertainties, although still acceptable, particularly between 8 and 11 s period. The fundamental mode will be accurate for periods less than about 21 s.

3.2 Demonstrating RT integration coupling

The first group of tests using the sets of forcing functions and Green's functions discussed above produced mode by mode hybrid results directly comparable to PPM synthetic single mode seismograms. PPM synthetic seismograms were calculated at $\Delta_s = 1600$ km for each of the fundamental mode and the first five overtones. For the fundamental mode and each of the first five overtones a set of single mode PM forcing functions, at $\Delta_s = 1500$ km, was combined with the corresponding single mode set of Green's functions, for a propagation distance of $\Delta_{RT} = 100$ km, according to the representation theorem integral. This produced a hybrid seismogram for that mode at $\Delta = 1600$ km to compare with the corresponding PPM single mode synthetic. Comparisons of the RT integration sums and the PPM synthetics for each individual mode are shown in Fig. 5. All the seismograms are bandpass filtered for periods between 1 and 25 s. The short period limit on the bandpass filter was chosen to improve the correspondence between the waveform of the PPM synthetic and the RT integration result for the same mode. The short period limit corresponds to the shortest period energy that can be transmitted through a finite element grid with grid spacing equal to the spacing of the

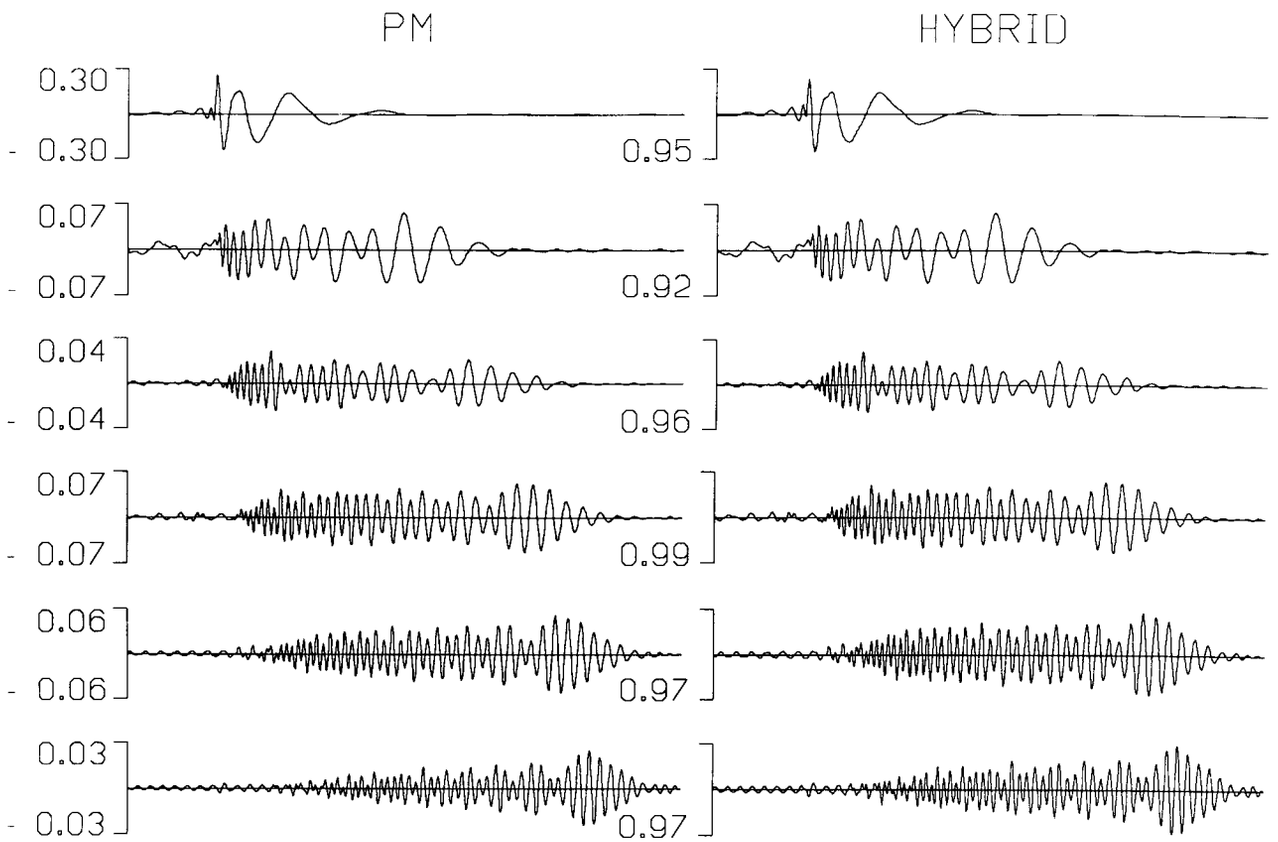

Figure 5. Mode by mode RT integration results bandpass filtered between 0.04 and 1 Hz. Two columns of seismograms are illustrated. The first column, labelled PM, shows PPM synthetics for each overtone and for the fundamental mode. The PPM synthetics are calculated for a line source at a depth of 8 km, at a distance $\Delta_s = 1600$ km from the source, using a single PM calculation. The second column, labelled hybrid, shows the hybrid synthetics for a PM path length of $\Delta_s = 1500$ km (line source) and a RT integration path length of $\Delta_{RT} = 100$ km. Each row of seismograms represent results for a different overtone. The first row shows the fundamental mode, the second row the first overtone, the third row the second overtone, the fourth row the third overtone, the fifth row the fourth overtone, and the sixth row the fifth overtone. Each row of seismograms is plotted using the same scaling. The numbers at the left hand edge of each row indicate the amplitude. The numbers between each pair of seismograms indicate the rms amplitude ratio of the hybrid seismogram to the PPM seismogram.

integration points in the RT integration. The long period cut-off of the filter is chosen to remove the long period component of the fundamental mode which cannot be accurately reconstituted without increasing F_1. When the integration surface is truncated at progressively shallower depths the long period cut-off of the filter must be progressively reduced to maintain the fit between hybrid and PPM fundamental mode seismograms. As F_1 is reduced below 50 km the correspondence between the hybrid and PPM overtone seismograms for each overtone degenerates. As predicted in the error analysis the largest discrepancies between the PPM and hybrid results, for $F_1 = 50$ km, occur in the first overtone seismograms. Some discrepancies are seen in the fundamental mode due to the longer periods between 21 and 25 s which are not removed by the filter. The higher overtones fit well and approach the accuracy predicted by the minimum error estimates above.

In practice a full mode sum seismogram is the desired result of representation theorem integration coupling. The mode by mode tests discussed above illustrate the validity of the method and illustrate our understanding of the sources of possible uncertainties. To illustrate the accuracy obtained using mode sum forcing functions and Green's functions the hybrid synthetic resulting from RT integration using mode

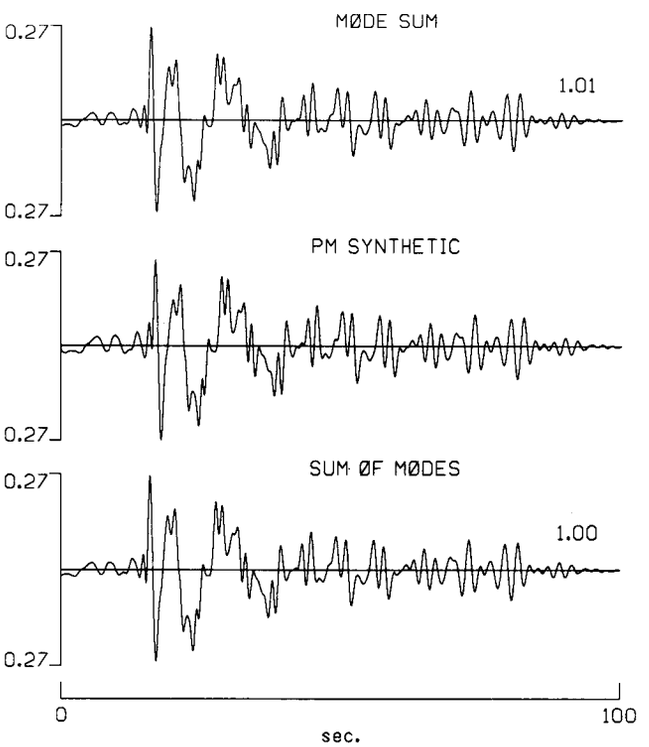

Figure 6. Mode sum RT integration results bandpass filtered between 0.04 and 1 Hz. The centre seismogram is a PPM seismogram for a line source at a depth of 8 km at a distance $\Delta_s = 1600$ km from the source. The upper-most and lower-most seismograms are hybrid seismograms for a PM (line source) path length of $\Delta_s = 1500$ km and a RT integration coupling path length of $\Delta_{RT} = 100$ km. The seismogram labelled mode sum was calculated using a single RT integration of mode sum, line source, forcing functions and mode sum Green's functions. The seismogram labelled sum of modes is a sum of the single mode RT integration results shown in Fig. 4.

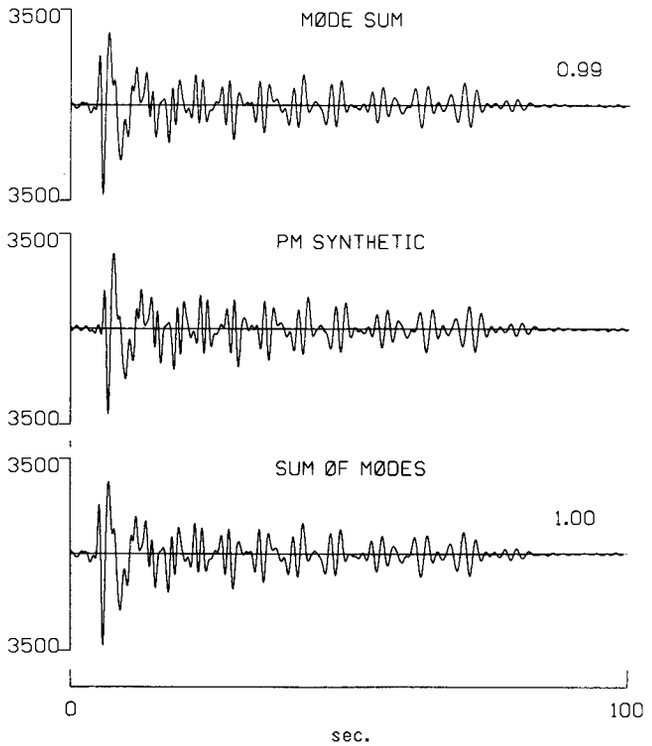

Figure 7. Mode sum RT integration results. PM seismograms are calculated for a strike-slip point double-couple source. Other details as in Fig. 6.

sum forcing functions and Green's functions is compared with the corresponding PPM mode sum synthetic. Fig. 6 shows results using a line source, and Fig. 7 shows results using a point source. The agreement in amplitude and waveform between the PPM and hybrid mode sum results is excellent. The sum of modes synthetic calculated as a sum over the single mode hybrid results shown in Fig. 5 gives a similar result. The agreement between the mode sum hybrid seismogram and the sum of single modes hybrid seismogram provides an independent check and the validity of the filtering technique, since any cross-terms that did not cancel due to orthogonality would appear as deviations between the two sets of resulting seismograms. That is, cross-terms present in the mode sum result would not be present in the sum of modes result.

3.3 Demonstration of Green's function filtering

Next, a series of calculations investigating the accuracy and efficiency of the Green's function filtering technique will be discussed. The Green's function filtering method uses Green's functions, containing only a subset of the modes present in the forcing functions, as a filter to extract only those modes from the forcing functions. In particular, the single mode sets of Green's functions are used in the representation theorem integral along with the mode sum set of forcing functions. The resulting hybrid seismograms contain energy only in the single mode present in the Green's function. A representation theorem integration was performed using each single mode set of Green's functions and the set of mode sum forcing functions. As an example results using the third higher mode Green's functions and a

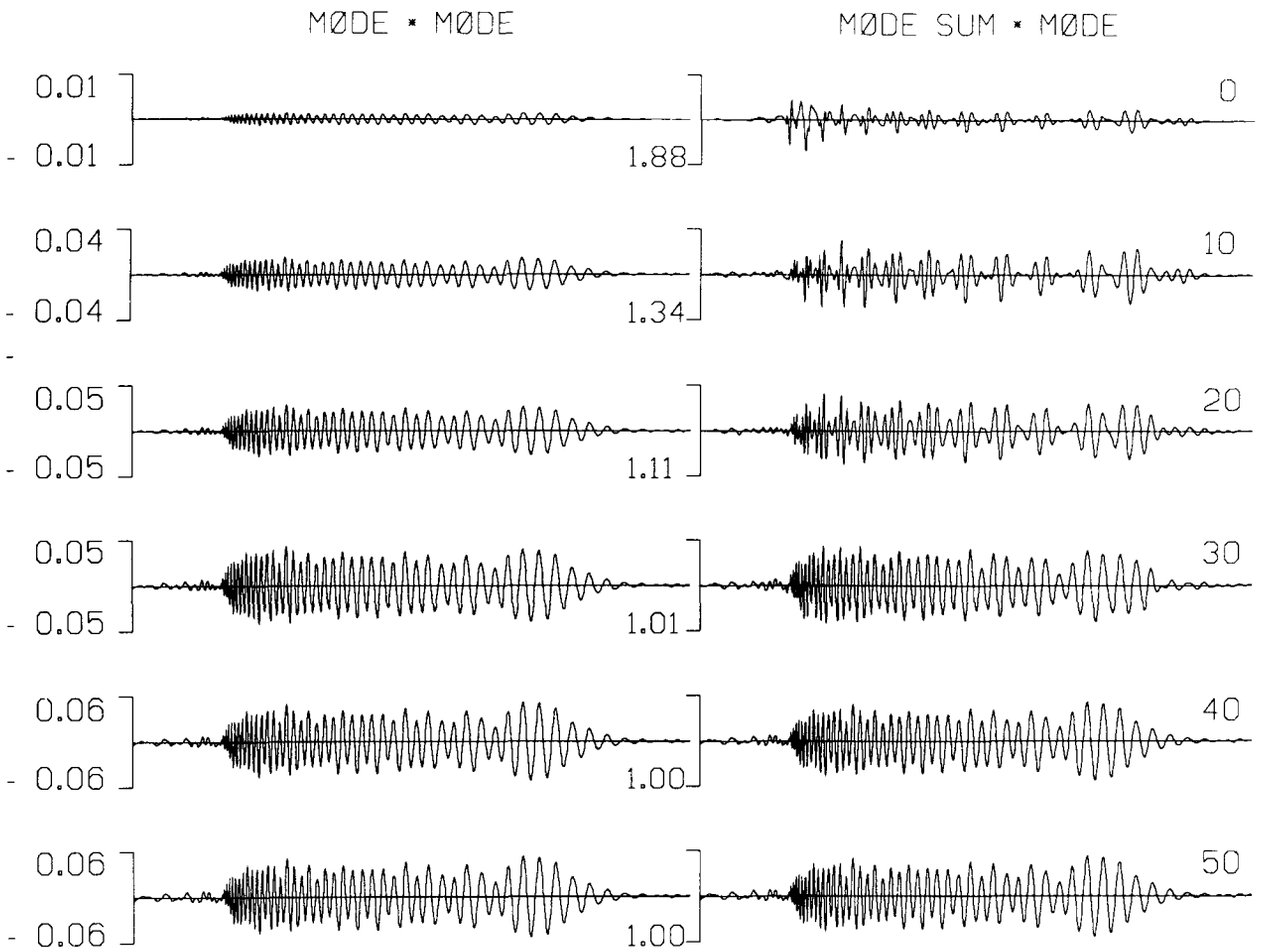

Figure 8. Green's function filtering using the third overtone as an example. All illustrated seismograms are bandpass filtered between 0.04 and 1 Hz. The results of a different RT integration are presented in each column. Both columns show hybrid seismograms for a line source at a depth of 8 km and a distance $\Delta_s + \Delta_{RT} = 1600$ km from the source. In both cases the PM path length is $\Delta_s = 1500$ km, and the RT integration path length is $\Delta_{RT} = 100$ km. In the first column, labelled mode * mode, the hybrid seismograms are derived using the third overtone forcing functions and the third overtone Green's functions. In the second column, labelled mode sum * mode, the hybrid seismograms are derived using the mode sum forcing functions and the third overtone Green's functions. Each pair of seismograms is plotted using the same scale, but the scale changes from pair to pair. The amplitude is indicated at the left end of each pair of seismograms. The RT integration begins at the surface and proceeds down FF_1 (Fig. 2) to F_1. The first row of seismograms is a single convolution, the sum down to a depth of 0.25 km. The second row is the sum of 21 convolutions, and includes all integration points to a depth of 10 km. This pattern continues with the depth of the deepest point included in the integration indicated to the right of each pair of seismograms. The numbers between the pairs of seismograms indicate the rms amplitude ratios of the mode sum * mode seismograms to the mode * mode seismograms.

line source are shown in Fig. 8. When a depth of $F_1 = 50$ km is reached the waveforms are indistinguishable and the amplitudes agree to within less than 1 per cent. Studying similar plots for each overtone and for the fundamental mode shows several trends that hold for both point sources and line sources. In general the integration must proceed to a depth F_1 of about 30 km before the waveforms of the filtered mode sum seismograms closely resemble those of the single mode hybrid results. For the third to fifth overtones the filtered results at $F_1 = 50$ km and the analytical results agree in amplitude (rms amplitude differ by <1 per cent) and are not visibly different in waveform. Integration over the full 50 km is necessary to stabilize the results. Integration to depths greater than 50 km does not improve the correspondence between hybrid and filtered results. For the first and second overtones integration to depths greater than 50 km improves the results slightly due to better fits at longer periods. For the fundamental mode increasing F_1 allows longer period energy to be modelled.

Fig. 9 illustrates the mode by mode results of the RT integrations discussed above for $F_1 = 50$ km. For the fundamental mode and all illustrated overtones the waveforms of the mode * mode hybrid results and the mode sum * mode results are essentially identical. The rms amplitude ratio of the two different types of hybrid result is one for each pair of seismograms shown. In fact even the peak-to-peak amplitudes agree to within less than 1 per cent for all modes. Clearly the Green's function filtering technique is accurate and promises to be very useful in the interpretation of hybrid seismograms for paths including complex structures. In summary, the effect of using a set of Green's functions containing a subset of the modes present

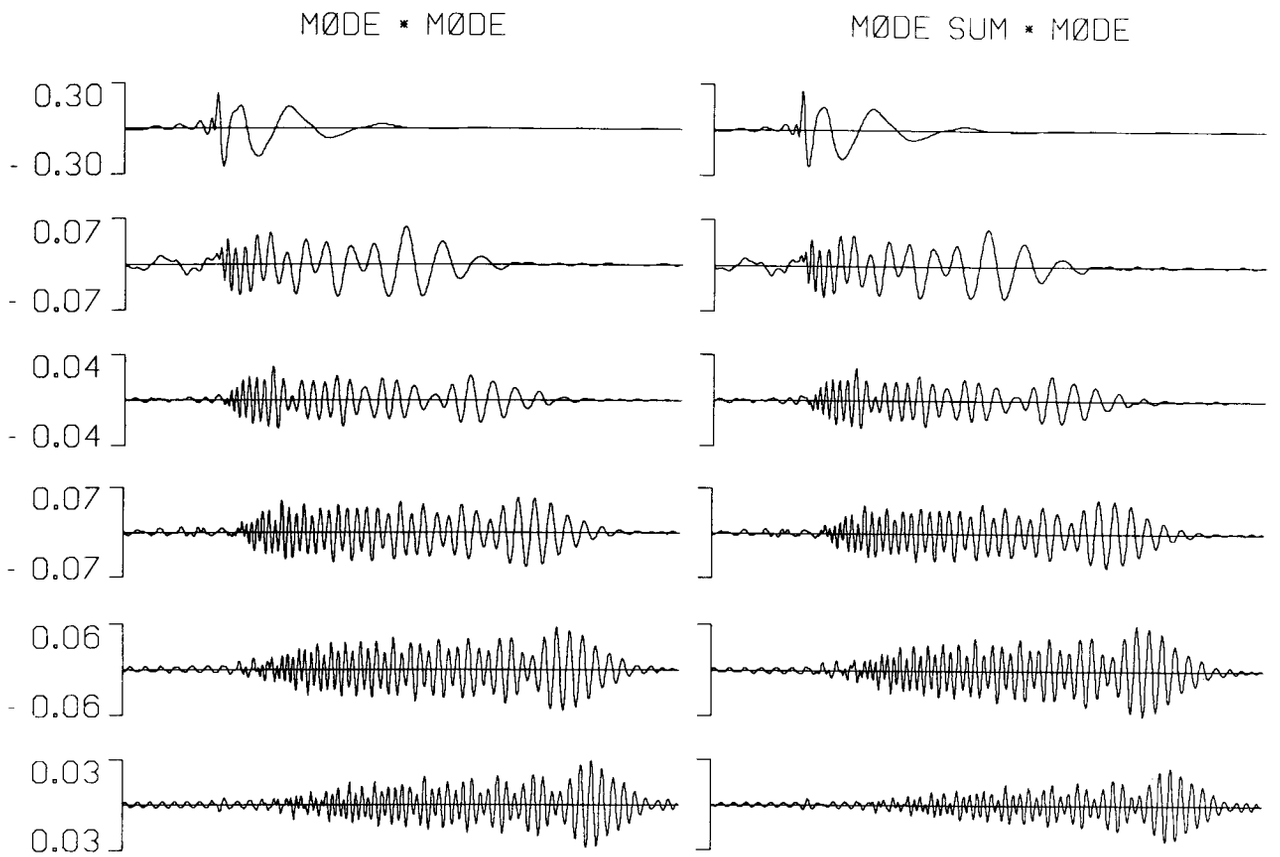

Figure 9. Mode by mode results of Green's function filtering. All seismograms are bandpass filtered between 0.04 and 1 Hz. The first row shows results for the fundamental mode, each successive row shows results for the next higher overtone. The results of a different RT integration are presented in each column. Both columns show hybrid seismograms for a line source at a depth of 8 km and a distance $\Delta_s + \Delta_{RT} = 1600$ km from the source. In both cases the PM path length is $\Delta_s = 1500$ km, and the RT integration path length is $\Delta_{RT} = 100$ km. In the first column, labelled mode * mode, the hybrid seismograms are derived using the single mode forcing functions and the single mode Green's functions for that same mode. In the second column, labelled mode sum * mode, the hybrid seismograms are derived using the mode sum forcing functions and the single mode Green's functions. The extent of the integration surface, F_1, is 50 km for all illustrated seismograms. The amplitude scale is given to the left of each pair of seismograms. The rms amplitude ratios of the mode sum * mode seismograms to the mode * mode seismograms is one in all cases and is thus not illustrated on the diagram.

in the set of forcing functions is to produce an efficient filter that allows only the modes common to both sets to appear in the hybrid result.

3.4 RT integration coupling and Green's function filtering using FE forcing functions

The examples of representation theorem integration coupling discussed to this point demonstrate the validity of coupling a wavefield expressed in terms of displacement seismograms, generated using the PM method, recorded at equal intervals along a vertical boundary, across that boundary. The wavefield is coupled across the boundary by RT integration, evaluation of equation (4) along that vertical surface, of the displacement seismograms and the appropriate line source Green's functions. It remains to be shown that RT integration coupling and Green's function filtering are valid when FE or FD displacement seismograms are used, and that the entire sequence of operations used to include a complex subsegment of a propagation path in that path is valid. The final example of RT coupling, presented in this section, addresses these questions.

The final example of RT coupling produces hybrid seismograms due to the propagation of energy from a source, through the first section of its path using the PM method, through the second section of its path using the FE method, and finally, through the last section of the path using RT integration coupling. Again, for this example, the entire path consists of a single simple plane-layered structure to allow direct comparison of the hybrid results to PPM results. A strike-slip double-couple point source at a depth of 8 km was used to generate a set of PM displacement seismograms along a vertical surface $\Delta_s =$ 1500 km from the source. The spacing between the points at which these seismograms were recorded was 0.5 km. Each of these seismograms was used as a displacement time history constraint on a grid point along the left-hand edge of a finite element grid with grid spacing 0.5 km. The application of this set of displacement time history constraints to the end of the finite element grid completely specified the motion of all nodes within the finite element grid for the duration of the FE calculation. At a column of nodes within the finite element grid displacement seismograms were recorded during the FE calculation. The

displacement seismograms were recorded at column 101, a distance $\Delta_s + \Delta_{FE} = 1550$ km from the source. These displacement seismograms were then used as forcing functions in a representation theorem integration. The distance propagated using representation theorem integration varied from 50 to 1000 km.

The results of the example described in the previous paragraph are illustrated in Fig. 10. The correspondence between the hybrid seismograms and the PPM seismograms is excellent. As the distance propagated using RT integration coupling increases the PPM seismograms appear to decay in amplitude faster than the hybrid seismograms despite the fact that the rms amplitude ratios remain relatively constant. This is an artefact of the fact that the rms amplitude ratio has the decay correction $\sqrt{\xi_1/x}$ from equation (12) included in it but the plotted seismograms are not scaled by the correction factor. This allows one to see the increasing importance of the 2-D to 3-D propagation correction as the portion of the path traversed using the 2-D finite element and representation theorem integration coupling techniques increases with respect to the portion of the path traversed using the 3-D propagator matrix propagation. The origin time of each seismogram in Fig. 10 is slightly different. When absolute times are considered the first peaks in each pair of seismograms align exactly.

Next, this example will be extended to present the results of a Green's function modal filtering of one of the hybrid seismograms in Fig. 10. The hybrid seismogram propagated $\Delta_{RT} = 100$ km using representation theorem integration is chosen for this analysis so that the single mode Green's functions already calculated can be used in the modal filtering analysis. The location at which this seismogram is recorded will be referred to as A. Since a single layer over a half-space structure is used for the entire path it is simple to predict that the transmission coefficients across the 'complex' region within the finite element grid should all be one and that the reflection coefficients should all be zero. Thus, the hybrid single mode seismograms recorded at A should be identical to the single mode PPM seismograms for a propagation path length of $\Delta_s = 1650$ km. Fig. 11 shows

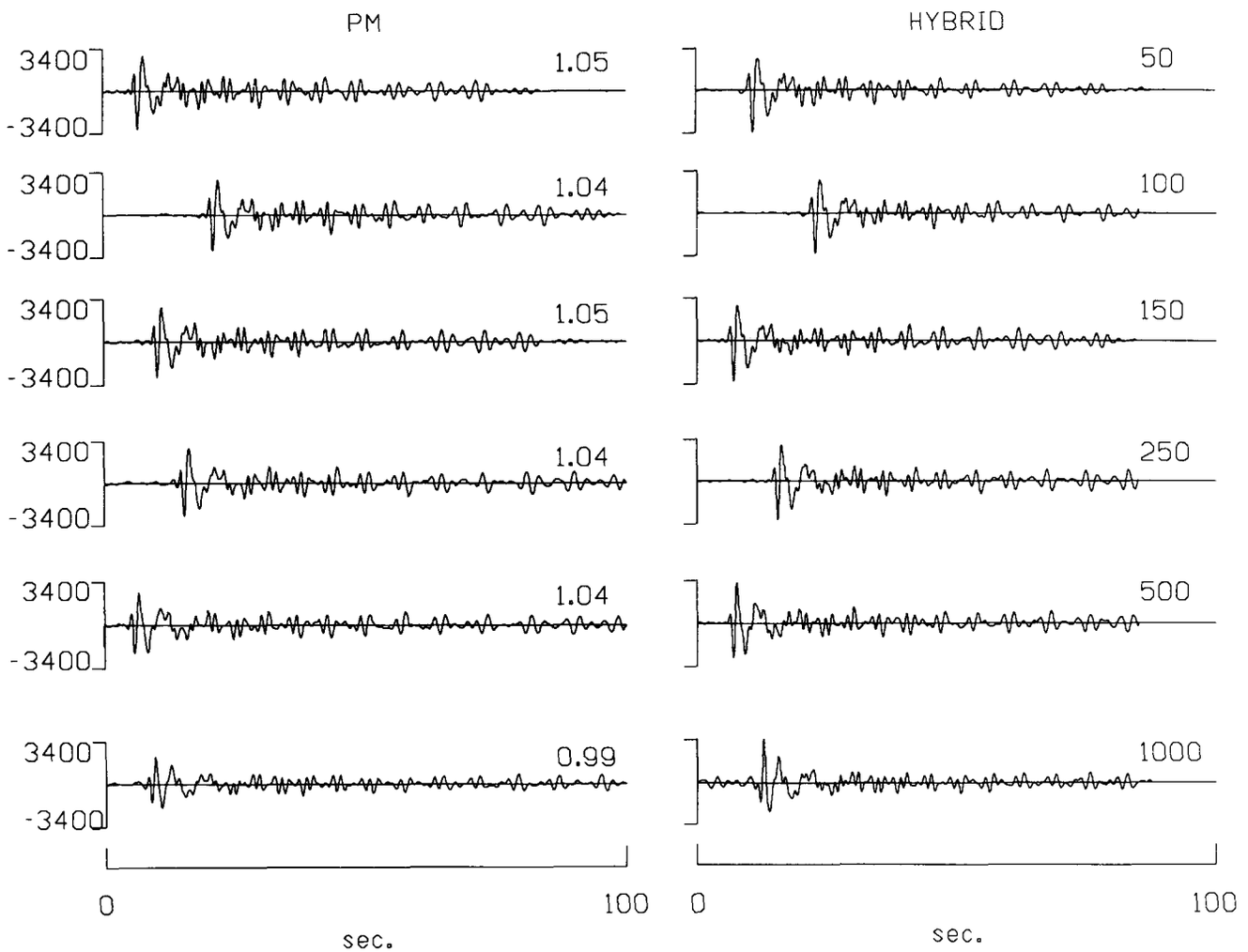

Figure 10. Mode sum RT results using FE forcing functions. All seismograms are bandpass filtered between 0.04 and 1 Hz. The first column show PPM results for each case, the second column shows the corresponding hybrid results. Each row illustrates results for a different propagation distance. For all hybrid seismograms the initial PM propagation distance from the source to the finite element grid edge is $\Delta_s = 1500$ km, and the propagation distance within the grid is $\Delta_{FE} = 50$ km. The distance, in kilometres, propagated using RT integration coupling, Δ_{RT}, is indicated to the right of each pair. The rms amplitude ratios of the hybrid results to the PPM results are shown between each pair of seismograms. Origin times of the plotted seismograms are arbitrary. Arrows below each seismogram indicate the arrival times.

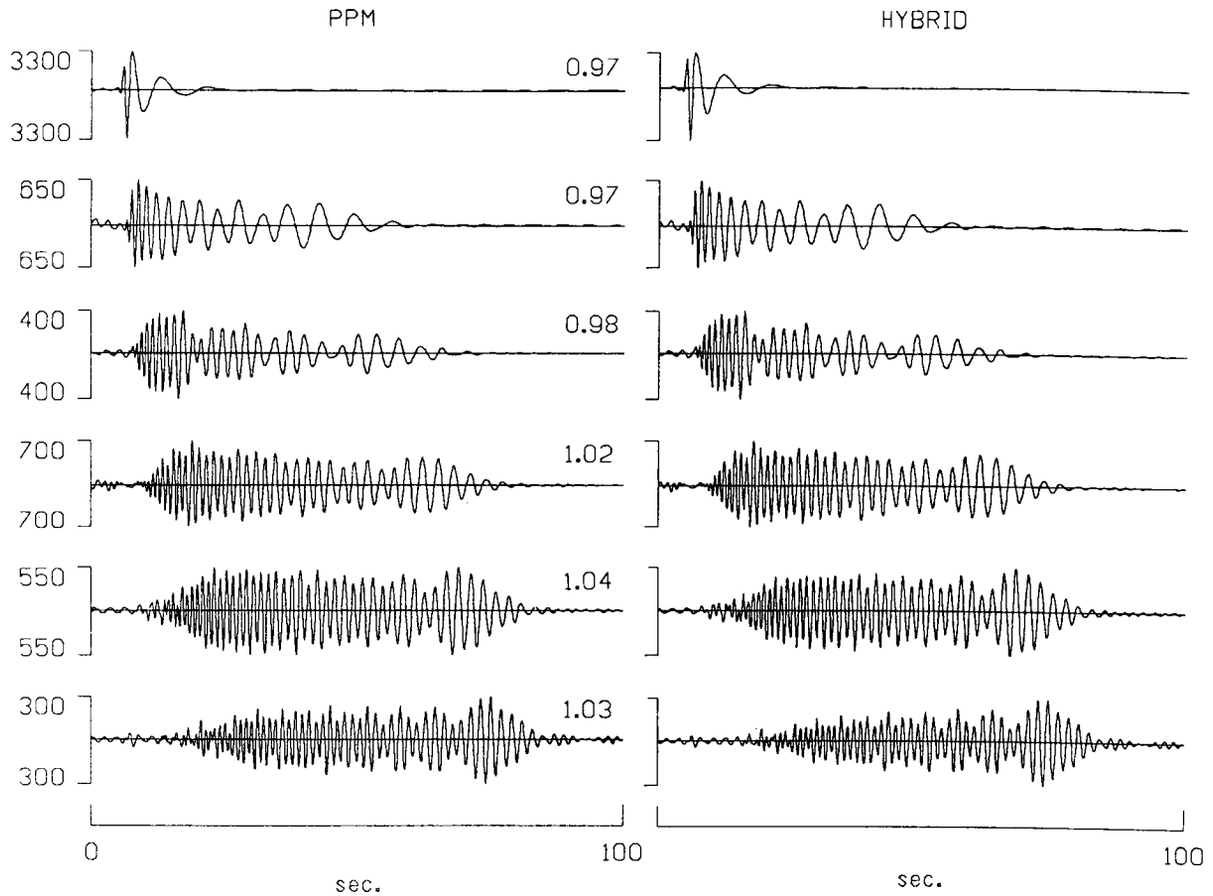

Figure 11. Example of Green's function filtering of hybrid synthetics. The hybrid seismogram for receiver A, with $\Delta_s = 1500$ km source to FE distance, $\Delta_{FE} = 50$ km FE propagation distance, and $\Delta_{RT} = 100$ km RT integration coupling propagation distance, shown in row 2 of Fig. 10 is analysed using mode by mode filtering. In the left-most column PPM seismograms for each single mode at receiver A are illustrated. In the right-most column hybrid filtered seismograms calculated using RT integration with the time series $u(A, t)$ recorded during the FE calculations as forcing functions and the single mode Green's functions for $\Delta_{FE} = 100$ km propagation are illustrated. The hybrid to PPM seismogram rms amplitude ratios are illustrated between each pair of seismograms. Amplitudes are shown to the left of each pair of seismograms.

mode by mode results which verify this. The hybrid single mode seismograms illustrated in Fig. 11 are calculated using the FE displacements, which contain modes on the fundamental and first five overtone branches, as forcing functions and single mode Green's functions.

For a real case the complex region within the finite element grid would produce mode to mode conversions and conversions to body waves which would cause non-unitary transmission coefficients and non-zero reflection coefficients. A modal analysis of a hybrid mode sum seismogram would require the calculation of the reflection and transmission coefficients for each mode. To determine the transmission coefficient the ratio of the hybrid seismogram to the PPM seismogram would be taken at a point which the wavefront reaches after propagating through the complex region. To determine the reflection coefficient the ratio of the energy in the seismogram resulting when the hybrid and PPM seismograms are differenced and the energy in the PPM seismogram would be taken at a point which the incident wavefront reaches before propagating through the complex region.

4 CONCLUSIONS

In this paper a method for propagating a mode sum wavefield through a long path containing short segments which include complex regions is presented. The wavefield is produced by a point double-couple or line source and is propagated from that source through a plane-layered medium to the edge of a mixed region using the propagator matrix method (PM). The mixed region must contain the complex region and small sections of the layered structures adjoining each end of the complex region. The wavefield is passed across the boundary between the plane-layered region and the mixed region using the technique discussed by Regan & Harkrider (1989). The wavefield is then propagated through the mixed region using the finite element (FE) method. After propagation through the mixed region, the FE wavefield is sampled at each node along a vertical surface. This surface must lie in the plane-layered region which the wavefield reaches after it has propagated through the complex region. The resulting seismograms are used as forcing functions in the representation theorem

integral which propagates the wavefield from the edge of the mixed region through the remainder of the second plane layered region.

In this paper the mathematical implementation of the representation theorem integration coupling method is developed and tested. A method of estimating the accuracy of the technique, based on the orthogonality of Love waves, is presented. Finally, the Green's function filtering technique for modal analysis of FE or hybrid results is derived and illustrated. A simple model which consists of a layer over a half-space is used for all sections of the propagation path in all tests described in this paper. This simple model allows the hybrid seismograms to be directly compared with seismograms generated using a single application of the propagator matrix method for the entire path (PPM). The agreement between hybrid seismograms and PPM seismograms for examples illustrated in this paper demonstrates the validity of the representation theorem integration coupling method. It shows that the method can produce hybrid synthetic seismograms of high accuracy. Evaluation of a simple expression derived from the expressions for the hybrid seismograms in propagator matrix notation and the corresponding expression of the orthogonality relation for Love waves allows one to evaluate the expected uncertainty for any single mode contribution to the hybrid seismogram. Evaluation of the uncertainty for each single frequency mode included in a mode sum seismogram has been demonstrated to be a good indicator of the sources of uncertainties in hybrid seismograms. The modal uncertainties have also been shown to provide an easily evaluated predictor of the vertical extent of the integration surface, and the minimum spacing between evaluation points on that surface, needed to provide a given level of accuracy. Results presented in this paper indicate that the Green's function filtering method provides accurate hybrid seismograms containing only those modes present in both the representation theorem integration forcing functions and the Green's functions used as a filter. Thus, single mode Green's functions yield hybrid results containing only a single mode.

ACKNOWLEDGMENTS

J. Regan conducted part of this research while a Canadian Government Laboratory Visiting Fellow at Geophysics Division, Geological Survey of Canada, Ottawa. This research was supported in part by the Advanced Research Projects Agency of the US Department of Defense and was monitored by the US Air Force Geophysics Laboratory under Contract F19628-87-K-0028. Division of Geological Sciences Contribution No. 4668. Geological Survey of Canada Contribution No. 30788.

REFERENCES

Aki, K. & Richards, P. G., 1980. *Quantitative Seismology,* W. H. Freeman, San Francisco.

Alsop, L., E., 1966. Transmission and reflection of Love waves at a vertical discontinuity, *J. geophys. Res.*, **71,** 3969–3984.

Alsop, L. E., 1968. An orthonormality relation for elastic body waves, *Bull. seism. Soc. Am.*, **58,** 1949–1954.

Boore, D., 1970. Love waves in nonuniform wave guides: finite difference calculations, *J. geophys. Res.*, **75,** 1512–1527.

Bose, S. K., 1975. Transmission of SH waves across a rectangular step, *Bull. seism. Soc. Am.*, **65,** 1779–1786.

Bouchon, M., 1981. A simple method to calculate Green's functions for elastic layered media, *Bull. seism. Soc. Am.*, **71,** 959–971.

Bouchon, M., 1982. The complete synthesis of seismic crustal phases at regional distances, *J. geophys. Res.*, **87,** 1735–1741.

de Hoop, A. T., 1958. Representation theorems for the displacement in an elastic solid and their application to elastodynamic diffraction theory, DSc thesis, Technische Hogeschool, Delft.

Drake, L. A., 1972. Love and Rayleigh waves in nonhorizontally layered media, *Bull. seism. Soc. Am.*, **62,** 1241–1258.

Drake, L. A. & Bolt, B. A., 1980. Love waves normally incident at a continental boundary, *Bull. seism. Soc. Am.* **70,** 1103–1123.

Frazier, G. A., Alexander, J. H. & Petersen, C. M., 1973. 3-D seismic code for the ILLIAC IV. *Systems, Science and Software Report SSS-R-73-1506.*

Gregersen, S. & Alsop, L. E., 1974. Amplitudes of horizontally refracted Love waves, *Bull. seism. Soc. Am.*, **64,** 535–553.

Gregersen, S. & Alsop, L. E., 1976. Mode conversion of Love waves at a continental margin, *Bull. seism. Soc. Am.*, **66,** 1855–1872.

Harkrider, D. G., 1964. Surface waves in multilayered media. Part I. Rayleigh and Love waves from buried sources in a multilayered elastic half-space, *Bull. seism. Soc. Am.*, **54,** 627–679.

Harkrider, D. G., 1970. Surface waves in multilayered elastic media, Part II. Higher mode spectra and spectral ratios from point sources in plane layered earth models, *Bull. seism. Soc. Am.*, **60,** 1937–1987.

Hudson, J. A. & Knopoff, L., 1964. Transmission and reflection of surface waves at a corner: I. Love waves, *J. geophys. Res.*, **69,** 275–280.

Kazi, M. H., 1978a. The Love wave scattering matrix for a continental margin (theoretical), *Geophys. J. R. astr. Soc.*, **52,** 25–44.

Kazi, M. H., 1978b. The Love wave scattering matrix for a continental margin (numerical), *Geophys. J. R. astr. Soc.*, **53,** 227–243.

Kennett, B. L. N., 1973. The interaction of seismic waves with horizontal velocity contrasts, *Geophys. J. R. astr. Soc.*, **33,** 431–450.

Kennett, B. L. N. & Mykkeltveit, S., 1984. Guided wave propagation in laterally varying media – II. L_g-waves in north-western Europe, *Geophys. J. R. astr. Soc.*, **79,** 257–267.

Knopoff, L. & Hudson, J. A., 1964. Transmission of Love waves past a continental margin, *J. geophys. Res.*, **69,** 1649–1653.

Knopoff, L. & Mal, A. K., 1967. Phase velocities of surface waves in the transition zone of continental margins – I. Love waves, *J. Geophys. Res.*, **72,** 1769–1776.

Knopoff, L., Mal, A. K., Alsop, L. E. & Phinney, R. A., 1970. A property of long-period Love waves, *J. geophys. Res.*, **75,** 4084–4086.

Kosloff, D. & Frazier, G. A., 1978. Treatment of hourglass patterns in lower order finite element codes, *Int. J. Numeric. Analyt. Method.*, **2,** 57–72.

Lysmer, J. & Drake, L. A., 1971. The propagation of Love waves across nonhorizontally layered structures, *Bull. seism. Soc. Am.*, **61,** 1233–1251.

Lysmer, J. & Drake, L. A., 1972. A finite element method for seismology, in *Methods in Computational Physics,* 11, *Seismology,* ch. 6, eds Alder, B., Fernbach, S. & Bolt, B. A., Academic Press.

Martel, L., 1980. Love wave propagation across a step by finite elements and spatial filtering, *Geophys. J. R. astr. Soc.*, **61,** 639–677.

Pec, K., 1967. Theoretical dispersion tables for Love waves propagating in a wedge and in a single nonhomogeneous layer with a linear velocity gradient, *Pub. Dominion Obs. Ottawa,* **35.**

Regan, J. & Harkrider, D. G., 1989. Numerical modelling of SH L_g waves in and near continental margins, *Geophys. J.*, in press.

Regan, J., 1987. Numerical studies of propagation of L_g waves across ocean continent boundaries using the representation theorem, *Ph D thesis,* California Institute of Technology, Pasadena, Ca.

Sato, R., 1961a. Love waves propagated across transitional zone, *Japan. J. Geophys.*, **2**, 117–134.
Sato, R., 1961b. Love waves in case the surface layer is variable in thickness, *J. Phys. Earth.*, **9**, 19–36.
Zienkiewicz, O. C. & Cheung, H., 1967. *The Finite Element Method in Structural and Continuum Mechanics*, McGraw-Hill, New York.

APPENDIX A

In this appendix the expression for SH displacement and stress at a receiver at depth z due to a source at depth h are presented in terms of Harkrider's (1964) propagator matrix notation. First strike-slip and dip-slip double-couple sources are considered, then line source results are given. Finally, line source Green function displacements and stresses are developed.

The displacement for an arbitrary double-couple source follows directly from the expression for the SH displacement at depth z produced by a double-couple source of arbitrary orientation at depth h (Harkrider 1964, 1970).

$$[v(r,\phi,z,\omega)] = 2\pi i K_{\#} k_\beta^2 \mu A_L \Bigg\{ \Big(\cos\lambda \sin\delta \cos 2\phi - \sin\frac{2\delta}{2} \sin 2\phi \Big) \Big[\frac{v_S(h)}{v_0}\Big]_H \frac{\partial H_2^{(2)}(k_L r)}{\partial r} - (\sin\lambda \cos 2\delta \cos\phi + \cos\lambda \cos\delta \sin\phi) \times \Big(\frac{1}{\mu(h)} \Big[\frac{\tau^*(h)}{\dot v_0/c_L}\Big]_H \Big) \frac{\partial H_1^{(2)}(k_L r)}{\partial r} \Bigg\} \Big[\frac{v_R(z)}{v_0}\Big]_H \tag{A1}$$

where

$$K_{\#} = \frac{-\bar M(\omega)}{4\pi\rho\omega^2} = \frac{iM_0}{4\pi\rho\omega^3} \qquad \dot v_0 = i\omega v_0 \tag{A2}$$

$$k_\beta^2 = \frac{\omega^2}{\beta^2} = \frac{\rho_s \omega^2}{\mu(h)} \qquad k_L = \frac{\omega}{c_L} \qquad \tau = i\tau^*. \tag{A3}$$

In equations (A1)–(A3), λ is the strike of the double-couple source, δ is the dip, ϕ is the azimuth to the station, β is the SH wave velcoity, ρ_s is the density at the depth of the source, h is the source depth, ω is the frequency, r is the distance from the source to the receiver, c_L is the Love wave velocity, $\mu(h)$ and $\mu(z)$ are respectively the rigidity at the source depth and at the receiver depth,

$$\Big[\frac{v_S(h)}{v_0}\Big]_H \quad \text{and} \quad \Big[\frac{\tau^*(h)}{\dot v_0/c_L}\Big]_H$$

are the terms that transmit the source disturbance in the z direction from the source to the surface,

$$\Big[\frac{v_R(z)}{v_0}\Big]_H$$

is the term that transmits the disruption in z from the surface to the receiver, and the term containing the Hankel function is the propagation term in the r direction. The source term is defined to contain all the angular dependence on δ, λ, and ϕ, as well as the term $2i\pi k_\beta^2 \mu K_{\#}$. The second equality in the first expression of equation (A2) assumes a step moment, that is $\bar M(\omega) = M_0/i\omega$.

It is well known that a double-couple of arbitrary orientation can be expressed in terms of a linear combination of double-couple sources of three types, vertical strike-slip ($\delta = 90°$, and $\lambda = 0°$), vertical dip-slip ($\delta = 90°$ and $\lambda = 90°$), and 45° dip-slip ($\delta = 45°$ and $\lambda = 90°$). Thus, results for these three fault types can be added to produce results for an arbitrary orientation, removing the necessity to repeat the entire procedure for each orientation to be studied. In fact, for SH waves, any fault geometry can be modelled using a linear combination of only the vertical dip-slip and the vertical strike-slip faults. Evaluating equation (A1) for each of these two fault types, yields the expressions used to determine displacement seismograms at a receiver at depth z due to a vertical strike-slip fault at depth h

$$[\bar v(r,z)] = -\frac{M_0}{2\omega} A_L \frac{\partial H_2^{(2)}(k_L r)}{\partial r} \Big[\frac{v_S(h)}{v_0}\Big]_H \Big[\frac{v_R(z)}{v_0}\Big]_H \tag{A4}$$

and due to a vertical dip-slip fault at depth h.

$$[\bar v(r,z)] = -\frac{M_0}{2\omega} A_L \frac{1}{\mu(h)} \frac{\partial H_1^{(2)}(k_L r)}{\partial r} \Big[\frac{\tau^*(h)}{\dot v_0/c_L}\Big]_H \Big[\frac{v_R(z)}{v_0}\Big]_H. \tag{A5}$$

The analytical expressions for the stress components for SH waves from a point double-couple source follow directly from these expressions. Only the final term in equations (A4) and (A5) depend directly on z. From Harkrider (1964)

$$\frac{\partial}{\partial z}\Big[\frac{v_R(z)}{v_0}\Big]_H = -\frac{k_L}{\mu(z)}\Big[\frac{\tau^*(z)}{\dot v_0/c_L}\Big]_H. \tag{A6}$$

All terms in equations (A4) and (A5) except the Hankel function are constant with respect to x. By expanding the Hankel function term in an asymptotic series for large r, and ignoring terms of order $1/r$, it can be shown that

$$\frac{\partial}{\partial r}\Big(\frac{\partial H_2^{(2)}(k_L r)}{\partial r}\Big) \approx -ik_L \frac{\partial H_2^{(2)}(k_L r)}{\partial r} \tag{A7}$$

Thus, taking the appropriate derivatives of the displacement expressions yields the expressions used to determine stress time histories at a receiver at depth z due to a vertical strike-slip fault at depth h

$$[\overline{\sigma_{zy}}(r,z)] = k_L \frac{M_0}{2\omega} A_L \frac{\partial H_2^{(2)}(k_L r)}{\partial r} \Big[\frac{v_S(h)}{v_0}\Big]_H \Big[\frac{\tau^*/(z)}{\dot v_0/c_L}\Big]_H \tag{A8a}$$

$$[\overline{\sigma_{xy}}(r,z)] = ik_L \mu(z) \frac{M_0}{2\omega} A_L \frac{\partial H_2^{(2)}(k_L r)}{\partial r} \Big[\frac{v_S(h)}{v_0}\Big]_H \Big[\frac{v_R(z)}{v_0}\Big]_H \tag{A8b}$$

and due to a vertical dip-slip fault at depth h.

$$[\overline{\sigma_{zy}}(r,z)] = k_L \frac{M_0}{2\omega} A_L \frac{1}{\mu(h)} \frac{\partial H_1^{(2)}(k_L r)}{\partial r} \Big[\frac{\tau^*(h)}{\dot v_0/c_L}\Big]_H \Big[\frac{\tau^*(z)}{\dot v_0/c_L}\Big]_H \tag{A9a}$$

$$[\overline{\sigma_{xy}}(r,z)] = \frac{ik_L \mu(z)}{\mu(h)} \frac{M_0}{2\omega} A_L \frac{\partial H_1^{(2)}(k_L r)}{\partial r} \Big[\frac{\tau^*(h)}{\dot v_0/c_L}\Big]_H \Big[\frac{v_R(z)}{v_0}\Big]_H. \tag{A9b}$$

The analytical expressions for stress due to a line source in a layered medium are found by a procedure similar to

that used above to obtain the stress expressions for the point double-couple source. The displacement at depth z due to a line source at depth h is

$$\{\bar{u}_y(x, z)\} = 2\pi i A_L \frac{\mu(h)}{k_L}\left[\frac{v_S(h)}{v_0}\right]_H\left[\frac{v_R(z)}{v_0}\right]_H e^{-ik_L x}. \quad \text{(A10)}$$

Therefore, the stresses for the 2-D line source are

$$[\overline{\sigma_{zy}}(x, z)] = -2\pi i\mu(h)A_L\left[\frac{v_S(h)}{v_0}\right]_H\left[\frac{\tau^*(z)}{\dot{v}_0/c_L}\right]_H e^{-ik_L x} \quad \text{(A11a)}$$

$$[\overline{\sigma_{xy}}(x, z)] = 2\pi\mu(h)\mu(z)A_L\left[\frac{v_S(h)}{v_0}\right]_H\left[\frac{v_R(z)}{v_0}\right]_H e^{-ik_L x}. \quad \text{(A11b)}$$

Applying the same treatment to the expression for the displacement Green's function for a line source in a layered half-space,

$$[\overline{\Gamma_{22}}(x, z; \xi_1, \xi_3)] = \frac{-i}{k_L}A_L\left[\frac{v_S(\xi_3)}{v_0}\right]_H\left[\frac{v_R(z)}{v_0}\right]_H e^{-ik_L(x-\xi_1)}, \quad \text{(A12)}$$

gives expressions for $\overline{\Gamma_{22,3}}$, and $\overline{\Gamma_{22,1}}$. In this case a stress source term rather than a stress receiver term is needed. Thus, the depth derivative is taken with respect to the source term. The form of the depth derivative is identical to that in equation (A6) except that z is replaced by h. Therefore the derivatives of the Green's function are

$$[\overline{\Gamma_{22,3}}(x, z; \xi_1, \xi_3)] = \frac{i}{\mu(\xi_3)}A_L\left[\frac{\tau^*(\xi_3)}{\dot{v}_0/c_L}\right]_H\left[\frac{v_R(z)}{v_0}\right]_H e^{-ik_L(x-\xi_1)} \quad \text{(A13a)}$$

$$[\overline{\Gamma_{22,1}}(x, z; \xi_1, \xi_3)] = -A_L\left[\frac{v_S(\xi_3)}{v_0}\right]_H\left[\frac{v_R(z)}{v_0}\right]_H e^{-ik_L(x-\xi_1)}. \quad \text{(A13b)}$$